Boosting Photoelectric Conductivity in Porphyrin-Based MOFs Incorporating C_{60}

Saied Md Pratik, Laura Gagliardi, Christopher J. Cramer**

Department of Chemistry, Minnesota Supercomputing Institute, and Chemical Theory Center, University of Minnesota, Minneapolis, Minnesota 55455, United States

Corresponding Authors

***E-mail:** gagliard@umn.edu and cramer@umn.edu.

Abstract:

Electronic structure calculations show that guest C_{60} in the porphyrin-containing metal organic frameworks Zn_2(TCPB)(DA-ZnP) (DA-MOF; H_4TCPB = 1,2,4,5-tetrakis(4-carboxyphenyl)benzene, DA-ZnP = [5,15-bis[(4-pyridyl)ethynyl]-10,20-diphenylporphinato]zinc(II)) and Zn_2(TCPB)(F-ZnP) (F-MOF; F-ZnP = [5,15-di(4-pyridyl)-10,20-bis(pentafluorophenyl)porphinato]-zinc(II)) engenders high photoelectrical conductivity due to efficient donor-acceptor charge transfer (CT) interactions. Structural modifications at the meso position of the porphyrin influence the preferred positions of C_{60} within the frameworks, giving rise to host-guest interactions with different anisotropic structural, electronic, and opto-electronic properties. A preferred slipped-parallel π-stacked interaction of C_{60} that is predicted for NH_2-substituted DA-MOF and F-MOF fosters strong charge-transfer (CT) transitions and lowers band gaps by ~1.0 eV compared to the pristine DA-MOF and F-MOF. Hopping rates computed using Marcus theory are found to be anisotropic and accelerated by multiple orders of magnitude across π-stacked interfaces created by C_{60} incorporation, a consequence of strong electronic coupling between initial and final diabatic states. Calculations indicate that photoinduced electron transfer (PET), as well as direct CT from porphyrin to C_{60} upon irradiation, triggers a charge separation process that leads to the formation of what should be long-lived electron-trapped states at the heterojunctions. Design principles revealed here for the control of photophysical and electron transfer processes will be useful for constructing new MOF-derived visible- and infrared-based optoelectronics.

Introduction

Metal organic frameworks (MOFs) are porous crystalline materials that have attracted extensive attention due to their wide-range of potential applications encompassing gas storage and separation, catalysis, chemical sensing, photocatalysis, and drug delivery.[1-9] Most MOFs are electrically insulating or poor conductors because of the insulating character of the organic ligands and/or energy mismatch or otherwise ineffective interaction between the ligand and metal orbitals (e.g., π−d interactions).[10-11] Intrinsic electrical conductivity or fast charge delocalization within the framework is the key to electrochemical applications.[12] Therefore, their implementation for such applications is significantly limited and further improving their electronic properties remains challenging.[13] While, structural regularity and synthetic flexibility of MOFs allow hierarchical and unambiguous assemblies of multiple chromophoric units and nodes, it remains a challenge to achieve a systematic structural-functional basis in MOFs that improves their electrical conductivity.[14-19] A detailed understanding of the nature of charge transport mechanisms in MOFs is vital to design the next generation of MOF-based optoelectronic materials.

Until recently, several experimental and theoretical reports have addressed the strategies to unlock the low energy charge transfer (CT) pathways within MOFs to engineer electrical conductivity -for example by utilization of redox active linkers,[15, 20] mixed valency,[21-23] formation of π-stacking with the MOFs,[24] and formulation of 2D π-conjugated MOFs.[25-26] An alternative strategy to induce electrical conductivity is to infiltrate the pores with an appropriate electron acceptor or donor that can facilitate host-guest CT interaction within the framework and introduce new pathways for carrier migration.[24, 27-29] In this context, Talin et al. reported that the electrical conductivity of benzentricarboxylate-based MOFs (HKUST-1) increased by six orders of magnitude by infiltrating it with tetracyanoquinodimethane (TCNQ), as the nitrile of TCNQ bridges Cu(II) sites and induces a continuous CT pathway throughout the MOF unit cell.[30] Farha and coworkers introduced electron deficient Nickel(IV) bis(dicarbollide) as a guest molecule in the microporous channel of NU-1000 MOF to facilitate donor-acceptor, interactions and the resulting MOF became electrically conductive.[31] Recently, covalent and non-covalent infiltrations of C_{60} in the pores of MOFs have received attention as they offer unique pathways for efficient CT from linker-based donors to the C_{60} acceptor and render the MOF electrically

conductive.[32-35] Hupp and coworkers have reported that the conductivity of NU-901 MOF increased substantially upon C_{60} incorporation due to CT from the pyrene-based linker to C_{60}.[32] Shustova and co-workers have integrated porphyrin and fullerene-based linkers within MOF scaffolds and demonstrated emergent photophysical and energy-transfer processes.[33] Very recently, Souto et al. reported that the electrical conductivity in a TTF-containing MOF (MUV-2) increased by ~2 orders of magnitude after C_{60} incorporation due to CT between C_{60} and the TTF-based framework.[36]

Porphyrins and metalloporphyrins have seen widespread use in the design of molecular optoelectronics owing to their exceptional photophysical, electrochemical, and structural properties.[37-39] Their installation as linkers in a rigid framework keeps them well separated and prevents self-quenching, while at the same time permitting utilization of the full range of porphyrin properties. Such architecture have the potential to unlock new pathways for solar light harvesting, energy transport and exciton migration.[40-42] Porphyrin derived MOFs are superior to their monomeric units and have been exploited for solar energy applications, in particular for the design of photovoltaics and photocatalysts.[43-45] As two recent examples, Hupp and coworkers have synthesized two zinc porphyrin-derived MOFs (Figure 1, a and b), Zn_2(TCPB)(DA-ZnP) (DA-MOF; H_4TCPB = 1,2,4,5-tetrakis(4-carboxyphenyl)benzene, DA-ZnP = [5,15-bis[(4-pyridyl)ethynyl]-10,20-diphenylporphinato]zinc(II)) and Zn_2(TCPB)(F-ZnP) (F-MOF; F-ZnP = [5,15-di(4-pyridyl)-10,20-bis(pentafluorophenyl)porphinato]-zinc(II)).[46] We are particularly interested in these two MOFs as the highly ordered arrangement of porphyrin units within their frameworks should facilitate long-distance and directional migration of photogenerated excitons, making them efficient for energy-transport and related applications. In a follow up study, these authors reported the light harvesting efficiency of DA-MOF and F-MOF to be enhanced upon incorporation of CdSe/ZnS core/shell quantum dots (QDs) because of energy transfer from the QDs to the MOFs.[47]

In this work, we systematically apply density functional theory (DFT) to study the structures of DA-MOF and F-MOF with incorporated C_{60} (referred to hereafter as C60@DA-MOF and C60@F-MOF, respectively) as well as photophysical and electron-transfer processes that occur therein. We show that electrical conductivity is significantly enhanced through efficient CT interactions from the porphyrin-based donor to the C_{60}-based acceptor. To improve

the degree of CT between the donor-acceptor conjugates, we also explore structural modifications at the meso position of the porphyrin, which are found to influence the preferred positioning of C_{60} within the crystallographic framework. We find that charge carrier mobility across π-stacked heterojunction interfaces increases by several orders of magnitude upon C_{60} doping. Finally, we demonstrate that the donor-acceptor interface readily promotes photoinduced electron transfer from porphyrin to C_{60}, allowing the formation of charge separated states that should make these heterostructures excellent platforms for designing optoelectronics.

Computational details:

First-principles calculations for structural optimizations were performed within the framework projector augmented wave (PAW) approach as implemented in the Vienna ab initio simulation package (VASP 5.4.4).[48] Electron exchange-correlation was incorporated by the generalized gradient approximation (GGA) employing semi-local PBEsol functional.[49] The ionic core-electron interactions were taken into account using ultrasoft pseudopotentials. During geometry optimization, all atomic positions were fully relaxed unless Hellman−Feynman forces become less than 0.05 eV/Å. A planewave kinetic energy cut-off of 500 eV and 2×2×2 k-point mesh was used with an electronic energy convergence criterion of 10^{-6} eV. Lattice parameters of the unit cell varies ~1.0% (Table S1) upon optimization with respect to the experimental CIFs which thereby justifying the choice of our level of calculations. Subsequent single-point calculations for band energies and densities of states were performed using the screened hybrid functional of Heyd, Scuseria and Ernzerhof (HSE06).[50] Dispersion interactions were taken into account employing Grimme's DFT-D3 empirical formalism.[51] We have incorporated one C_{60} per unit cell and the binding energy (ΔE) within the MOF scaffolds was computed as $\Delta E = E(C_{60}$ incorporated MOF)−E(MOF) −E(C_{60}).

Time-dependent DFT (TD-DFT) calculations using HSE06 were performed on cluster models as retrieved from each of the system containing bare porphyrin-based linkers and C_{60}. The 6-31+G(d) basis set was used for C, H, N and F, while for the Zn Stuttgart−Dresden−Dunning (SDD) pseudopotential was employed.[52-53] The singlet–singlet excitations were modeled considering 100 excited states. These calculations were performed using Gaussian 16 suite of programs.[54]

Charge transfer integral (or electronic coupling) calculations were carried out on cluster models, chosen on the basis of center to center distances between the neighboring molecules in each system. These calculations were performed using the fragment approach as implemented in the Amsterdam density functional (ADF) package[55-56] with the M06-2X[57] functional and the TZP all-electron basis set.

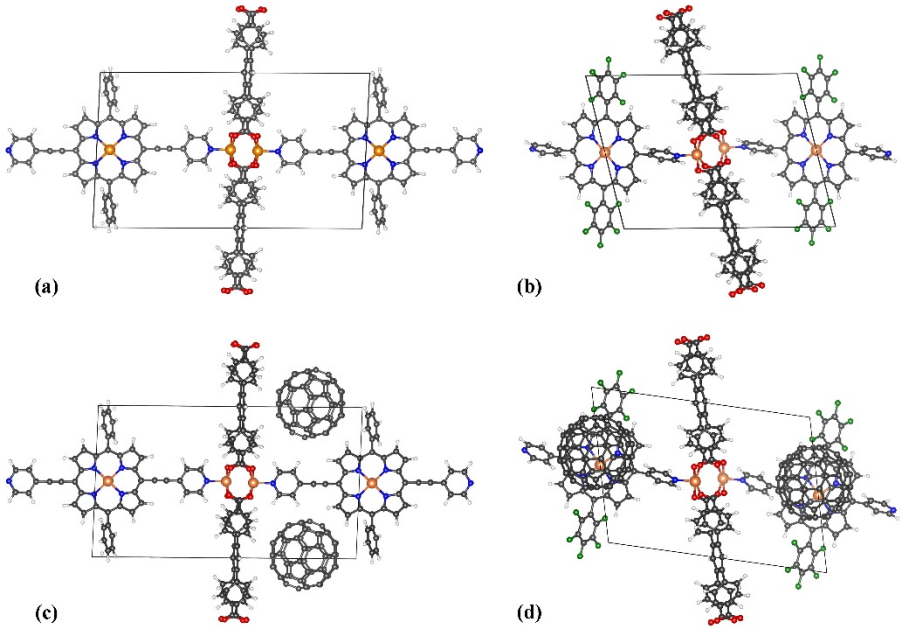

Figure 1. Optimized crystal structures of (a) DA-MOF and (b) F-MOF. (c) and (d) are their C_{60} incorporated analogues. Atomic colors are H (white), C (gray), N (blue), O (red), F (blue-green), and Zn (orange).

Results and Discussion

Both DA-MOF and F-MOF contain zinc porphyrin cores as photoactive building blocks and their meso positions (10- and 20- positions) can accommodate "out of plane" phenyl and pentafluorophenyl substituents, respectively (Figure S1 in SI). In contrast to F-MOF, DA-MOF possesses extended conjugation through the incorporation of two additional acetylene moieties at the 5- and 15- positions which makes the pyridine units coplanar with the porphyrin (Figure S1 in SI) and increases the pore size as well. Our calculations indicate that C_{60} can be incorporated

in the pore channel of DA-MOF only through edge-on interaction (Figure 1c), while in F-MOF C_{60} can be incorporated in between two co-facial porphyrin moieties, leading to a complete π-stacked arrangement (Figure 1d). Optimized lattice parameters following C_{60} incorporation are almost unchanged for DA-MOF, but change significantly for F-MOF (Table S1 in SI). While this suggests that there may be some kinetic barrier to the incorporation of C_{60} in the latter, the C_{60} binding energies (ΔE) computed at the PBEsol-D3 level are -1.23 eV and -1.32 eV for DA-MOF and F-MOF, respectively, suggesting that incorporation is quite favorable in both instances. The higher binding energy in F-MOF is consistent with the better aligned π–π stacking interactions between the porphyrin and C_{60} in its case. Such strong C_{60} binding energies are consistent with dispersion type interactions reported for fullerene encapsulated porphyrin-based cage complexes.[58]

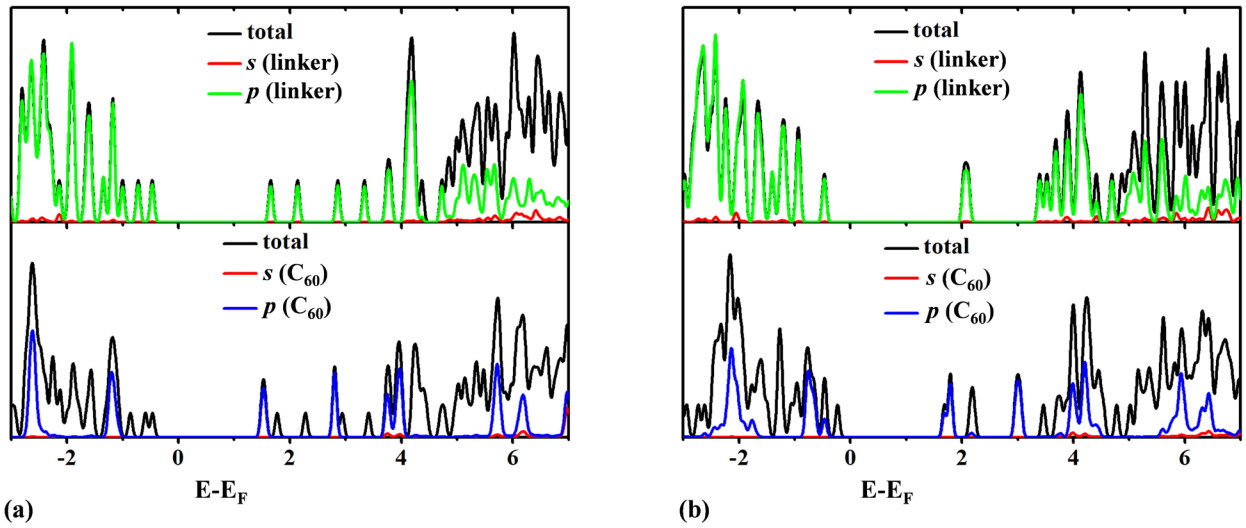

Figure 2. Calculated density of states for (a) DA-MOF and (b) F-MOF, before (upper panel) and after (lower panel) C_{60} incorporation. The energy is relative to the Fermi level and the *y* axis for the *s*- and *p*-orbitals is scaled by a factor 1.75.

To understand the influence of C_{60} incorporation, we have calculated the total density of states (TDOS) for DA-MOF and F-MOF before and after incorporation of C_{60} (Figure 2). Calculated optical band gaps (E_g) for DA-MOF and F-MOF are 1.66 eV and 2.04 eV,

respectively, which is in the visible region as expected for the porphyrin-based linkers. Partial density of states (PDOS) analysis reveals that both the highest occupied crystal orbitals (HOCO) and lowest unoccupied crystal orbitals (LUCO) predominantly comprise the p-orbitals of the linkers, and thus the absorption and emission properties of both MOFs are mainly governed by the electronic structure of the linkers (Figure 2, upper panels and Figure S1.b). The band gaps in C_{60}@DA-MOF and C_{60}@F-MOF (Figure 2, lower panels) are 1.50 eV and 1.68 eV, respectively, which values are 0.16 eV and 0.36 eV lower than those of the undoped DA-MOF and F-MOF. Though the band gap reduction is not large, the heterostructures possess delocalized electronic states, where the HOCO mainly comprises p-orbitals of the linkers and the LUCO predominantly comprises p-orbitals of C_{60} (lower panels of Figure 2). There is significant orbital overlap between them as is important for typical donor-acceptor based CT complexes.[32] This indicates that photoelectrons and holes generated on the linker should readily transfer to C_{60} at the interfacial region (vide infra for cluster calculations that further explore this).

To further engineer the physicochemical properties of these species, we removed the "out of plane" (perfluoro)phenyl rings from the meso positions of the porphyrins in (F)DA-MOF to assess the effect on donor-acceptor conjugate structures. The resulting MOFs are referred to as H_DA-MOF and H_F-MOF, respectively (Figure S2). Since this operation creates additional void space within the pore channel, different polymorphs of C_{60}@H_DA-MOF and C_{60}@H_F-MOF become possible. For C_{60}@H_DA-MOF, we found three polymorphs, Type-I, Type-II, and Type-III, while for C_{60}@H_F-MOF we found only two, Type-A and Type-B (Figure 3). Similar to the parent C_{60}@DA-MOF, Type-I possesses an edge-on interaction between the porphyrin and C_{60}. In Type-II, C_{60} is incorporated between two co-facial porphyrin moieties to generate a complete π-stacking interaction and a double-decker complex. In Type-III, C_{60} is positioned in between two diagonally disposed porphyrin linkers, resulting in a slipped π-stacked complex. The lattice parameters for Type-I and Type-III C_{60}@H_DA-MOF remain almost unchanged compared to H_DA-MOF, while they expand slightly along the stacking direction in Type-II C_{60}@H_DA-MOF to accommodate C_{60} (Table S1). The computed binding energies (ΔE) of C_{60} in Type-I, Type-II, and Type-III are -0.91 eV, -1.16 eV and -0.89 eV, respectively. The larger ΔE in Type-II presumably results from the optimal π–π stacking interaction between the donor-acceptor conjugates.

Type-A for C_{60}@H_F-MOF shows complete π–π stacking interactions as is found in parent C_{60}@F-MOF, while Type-B has slipped stacked interactions between the porphyrin and C_{60}. The binding energy of C_{60} in Type-A is larger than in Type-B (-1.37 eV vs -1.11 eV) again owing to better π–π interactions in the former.

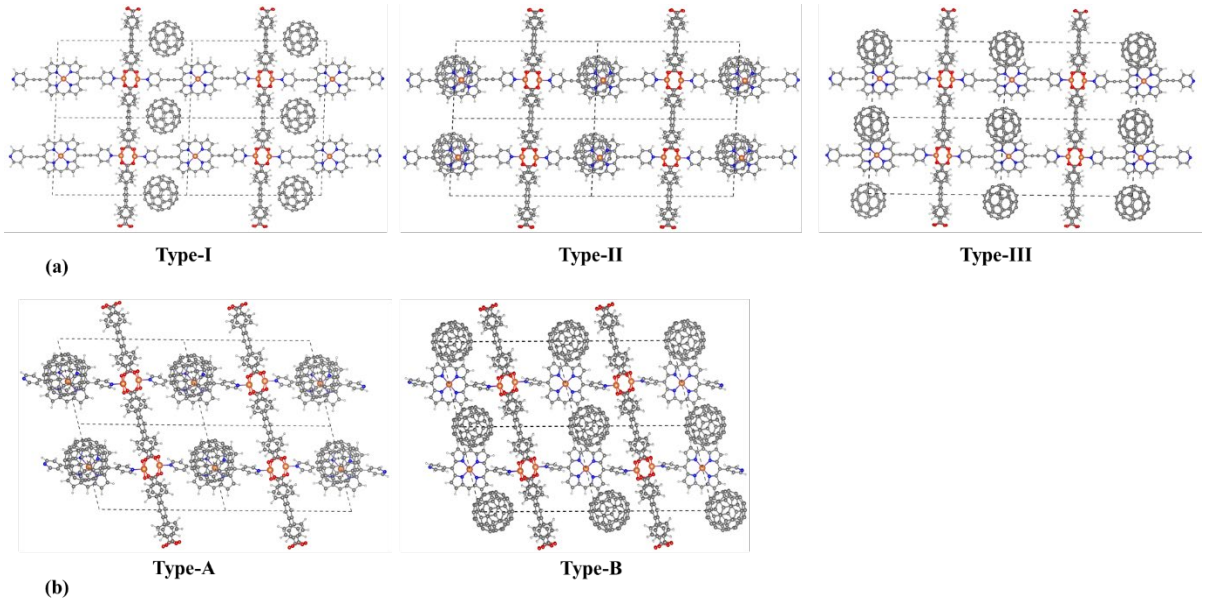

Figure 3. Different crystallographic packing arrangements of C_{60} within the pore channel of (a) H_DA-MOF and (b) H_F-MOF shown using a 2×2×2 supercell. The dashed line represents the unit cell. See caption to Figure 1 for atomic colors.

H_DA-MOF has a similar density of states and band gap (1.69 eV) as DA-MOF (1.66 eV) (Table 1, Figure S3), indicating that the diphenyl rings in the meso position have a negligible effect on the band gap. By contrast, H_F-MOF has an increased band gap (2.34 eV) compared to F-MOF (2.04 eV) following the removal of the pentafluorophenyl substituents. The computed band gaps of Type-I, Type-II, and Type-III of C_{60}@H_DA-MOF are lower by ~0.2-0.4 eV compared to H_DA-MOF, while C_{60}@H_F-MOF has band gaps lower by 0.63 eV and 0.77 eV in Type-A and Type-B, respectively, compared to H_F-MOF. While the excitations in H_DA- and H_F-MOFs are localized in nature and assignable as intramolecular π–π* transitions, their C_{60} encapsulated analogues access delocalized electronic states, where the HOCOs and LUCOs comprise p-orbitals of the linkers and C_{60}, respectively.

Table 1. Computed band gaps (E_g, eV) and binding energies (ΔE, eV) for DA-MOF, F-MOF, and their analogues after C_{60} incorporation.

MOFs	E_g for Free MOF	E_g (and ΔE) for C_{60}@MOF		
		Type-I	Type-II	Type-III
DA-MOF	1.66	1.50 (-1.23)		
H_DA-MOF	1.69	1.49 (-0.91)	1.54 (-1.16)	1.29 (-0.89)
NH_2_DA-MOF	1.30	0.85 (-1.06)	1.10 (-1.31)	0.71 (-0.94)
		Type-A		Type-B
F_MOF	2.04	1.68 (-1.33)		
H_F-MOF	2.34	1.71 (-1.37)		1.57 (-1.11)
NH_2_F-MOF	1.66	1.03 (-1.45)		0.67 (-1.36)

The photophysical properties of porphyrin are known to be sensitive to substitution of the meso position with electron-donating or accepting groups.[59] We considered the strong electron donor -NH_2 as such a group and computed the structures of NH_2_DA-MOF and NH_2_F-MOF, respectively (Figure S4) as well as C_{60}@NH_2_DA-MOF and C_{60}@NH_2_F-MOF, both of which were found to have the same number of polymorphs as their H-MOF analogs (Figure S5 and S6). The calculated C_{60} binding energies for NH_2_DA-MOF are -1.06 eV, -1.31 eV, and -0.94 eV for the Type-I, Type-II, and Type-III polymorphs, respectively, while for NH_2_F-MOF they are -1.45 eV and -1.36 eV for Type-A and Type-B, respectively. More complete π-π overlap in both Type-II and Type-A interfaces again leads to the highest binding energies. Compared to H_DA-MOF and H_F-MOF, the C_{60} binding energies are significantly higher in the NH_2-substituted cases (Table1), consistent with increased donor-acceptor interactions between the linkers and C_{60} that have the potential to impart more interesting optoelectronic properties.

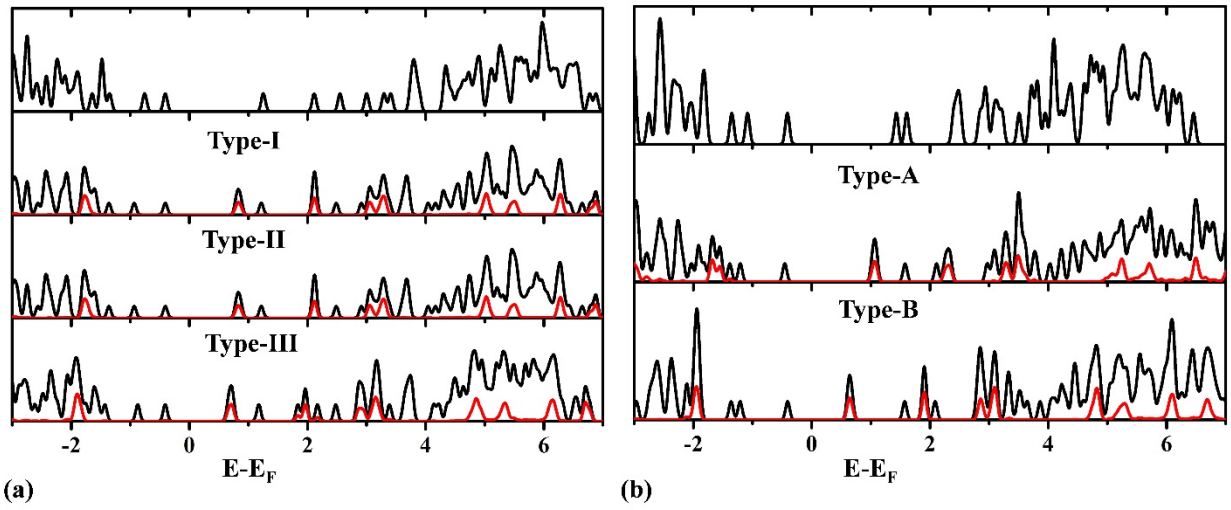

Figure 4. Calculated TDOS for (a) NH_2_DA and (b) NH_2_F-MOF are shown in upper panels (contribution from *s*- and *p*-orbitals and -NH_2 are given in Figure S7). In other panels TDOS (black line) and PDOS of C_{60} (red line) for different polymorphs are shown. The energy is relative to the Fermi energy.

Amine functionalization affects the electronic properties of the NH_2_MOFs (Figures 4, S7). The band gaps decrease by ~0.39 eV and ~0.68 eV, respectively, compared to H_DA-MOF and H_F-MOF (Table 1). PDOS analysis indicates that low-energy optical transitions are intralinker π–π* absorptions (Figure S7). The band gaps of the Type-I, Type-II, and Type-III polymorphs of C_{60}@NH_2_DA-MOF are 0.85, 1.10 and 0.71 eV, respectively, which values are lower than that for NH_2_DA-MOF by 0.45, 0.21 and 0.59 eV, respectively. Similarly, the band gaps of Type-A and Type-B (1.03 eV and 0.67 eV, respectively) are lower (by 0.63 and 0.99 eV, respectively) than that of NH_2_F-MOF. The incorporation of C_{60} in NH_2_DA-MOF and NH_2_F-MOF thus leads to infrared-bandgap tuned materials, again with delocalized electronic states that should permit efficient charge transfer across interfacial regions leading to improved electrical conductivity.

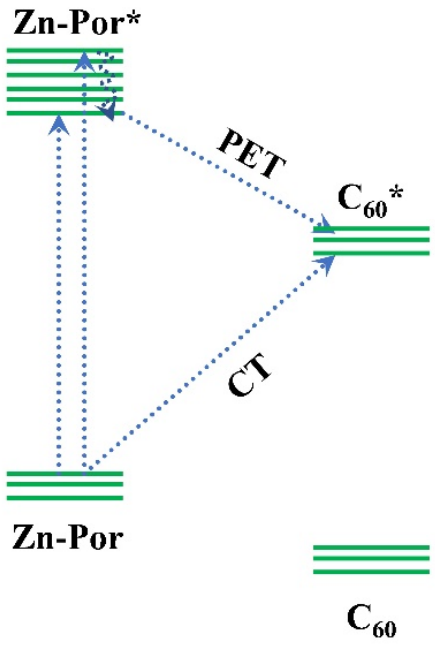

Scheme 1. Schematic representation for direct charge transfer (CT) and photoinduced electron transfer (PET) processes between porphyrin-based donor and C_{60} based acceptor.

Our solid-state electronic structures indicate that the empty states of C_{60} are positioned in between the band extrema of the empty MOFs. In addition, several donor-acceptor conjugates have geometries consistent with strong π–π interactions, which should facilitate charge transfer (CT) and photoinduced electron transfer (PET) processes from porphyrin to C_{60} (Scheme 1), which phenomena are well known for analogous molecular and supramolecular architectures.[60-61] To obtain further insight into the localized character of these electronic processes, we performed time dependent DFT (TD-DFT) calculations on cluster models of bare linkers and C_{60} extracted from our systems. Each C_{60} is in close proximity to four porphyrin units within the framework and we have decomposed the system into corresponding fragments accordingly (see Section S2 of SI). We restrict discussion here to results from C_{60}@NH_2_DA-MOF Type-III and C_{60}@NH_2_F-MOF Type-B, as minimum band gaps are predicted for these systems; details for other systems may be found in the SI.

The cluster model of C_{60}@NH_2_DA-MOF Type-III may be split into two fragments, namely, stacked, and diagonal, while for C_{60}@NH_2_F-MOF Type-B, three fragments are considered, namely, stacked, diagonal and parallel. Figure 5 shows that in the stacked fragment of C_{60}@NH_2_DA-MOF Type-III, the highest-energy occupied frontier orbitals are mainly

localized on the porphyrin while the lowest-energy unoccupied frontier orbitals are localized on both C_{60} and the porphyrin. The nature of the excited states, their associated vertical excitation energies ($E_{0\text{-}n}$), oscillator strengths (*f*), and the molecular orbitals (MOs) computed to dominate the transition are reported in Table 2. In the stacked fragment, low energy near IR transitions such as $S_0 \rightarrow S_1$ ($E_{0\text{-}1}$*= 0.62 eV; f=0.0003*), $S_0 \rightarrow S_2$ ($E_{0\text{-}2}$*= 0.67 eV; f=0.0047*), $S_0 \rightarrow S_3$ ($E_{0\text{-}3}$*= 0.69 eV; f=0.0054*), and $S_0 \rightarrow S_6$ ($E_{0\text{-}6}$*= 0.83 eV; f=0.0312*) occur from HOMO and HOMO-1 localized over the porphyrin to LUMO, LUMO+1, and LUMO+2 localized on C_{60}, indicating the direct CT nature of these excitations. This is consistent with the periodic calculations that predict the band gap for C_{60}@NH_2_DA-MOF Type-III to involve a porphyrin-based HOCO and a C_{60}-based LUCO. In contrast, higher energy intense transitions, e.g., $S_0 \rightarrow S_9$ ($E_{0\text{-}9}$*= 1.59 eV; f=0.0524*), $S_0 \rightarrow S_{10}$ ($E_{0\text{-}10}$*= 1.62 eV; f=1.0257*), and $S_0 \rightarrow S_{92}$ ($E_{0\text{-}92}$*= 2.98 eV; f=0.3585*) involve visible-light excitation and correspond to intramolecular $\pi \rightarrow \pi^*$ transitions within the porphyrin moiety (Table 2 and Figure 5). These higher-energy states should rapidly internally convert to the lowest-lying porphyrin-based excited state (Kasha's rule, Scheme1), and subsequent electron transfer to the LUMO of C_{60} would constitute a PET process facilitated by suitable spatial and geometric overlap in the donor-acceptor conjugate. A similar situation is found for the diagonal fragment of C60@NH_2_DA-MOF Type-III, with low-lying absorptions ascribed as direct CT excitations and higher energy absorptions associated with $\pi \rightarrow \pi^*$ transitions in the porphyrin moieties (Table S11 and Figure S24).

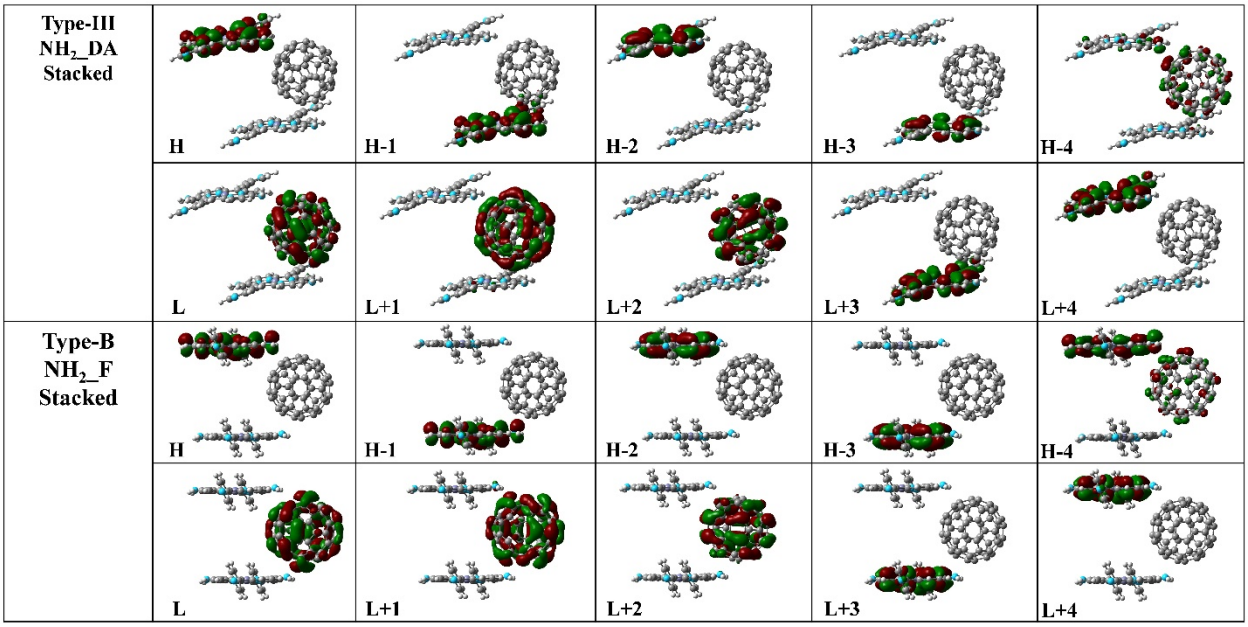

Figure 5. Frontier molecular orbitals for stacked fragments extracted from Type-III and Type-B polymorphs of C_{60}@NH_2_DA-MOF and C_{60}@NH_2_F-MOF, respectively (H = HOMO, L = LUMO). See caption to Figure 1 for atomic colors.

For C_{60}@NH_2_F-MOF Type-B, excitations are found to be similar to those for C_{60}@NH_2_DA-MOF Type-III. In the stacked fragment, lower energy transitions $S_0 \rightarrow S_2$ ($E_{0\text{-}2}$= *0.55 eV; f=0.0034*), $S_0 \rightarrow S_3$ ($E_{0\text{-}3}$= *0.59 eV; f=0.0263*), $S_0 \rightarrow S_4$ ($E_{0\text{-}4}$= *0.60 eV; f=0.0152*), $S_0 \rightarrow S_6$ ($E_{0\text{-}6}$= *0.66 eV; f=0.0288*) occur from porphyrin localized HOMO, HOMO-1 and HOMO-2 to C_{60} based LUMO, LUMO+1 and LUMO+2 (Table 2 and Figure 5), while higher energy transitions $S_0 \rightarrow S_{21}$ ($E_{0\text{-}21}$= *1.91 eV; f=0.0852*), $S_0 \rightarrow S_{22}$ ($E_{0\text{-}22}$= *1.93 eV; f=0.2893*), and $S_0 \rightarrow S_{34}$ ($E_{0\text{-}34}$= *2.19 eV; f=0.0288*) are molecular in nature on the porphyrin but should permit electron flow from $\pi \rightarrow \pi^* \rightarrow C_{60\text{-LUMO}}$. The diagonal and parallel fragments of C_{60}@NH_2_F-MOF Type-B are also similar (Table S13 and Figure S26). We investigated analogous electronic excitations for parent C_{60}@DA- and C_{60}@F-MOFs, as well as for all the other polymorphs of C_{60}@H_ and C_{60}@NH_2_ DA- and F-MOFs (see Section S2 of SI).

Interestingly, edge-on interactions between porphyrins and C_{60} in Type-I interfaces found in both H_DA- and NH_2_DA-MOF fail to permit direct CT, although PET is energetically allowed (Figures S17 and S22; Tables S4 and S9), which emphasizes the importance of the

crystallographic position of C_{60} in the MOF pore with respect to controlling the electronic processes taking place at the host-guest interfaces. Geometry notwithstanding, molecular and supramolecular assemble of porphyrin and fullerene are well known to engender long-lived radical cations and radical anions following photolysis.[60, 62] For instance, Chen et. al. recently reported that C_{60} spatially confined via covalent anchoring within the nanochannels of a porphyrin based covalent organic framework ([C_{60}]y-ZnPc-COFs, where y = acceptor content) promotes photoinduced electron transfer and allows charge separation to form $ZnPc^{\bullet+}$ and $C_{60}^{\bullet-}$species, and the resulting COF shows photoelectric conductivity.[34] Similarly, the C_{60}@DA-MOF and C_{60}@F-MOFs and their analogues reported here could allow the formation of ionized species that could contribute to photoelectric conductivity.

Table 2. Excited State, excitation energies (eV), wavelength (nm), oscillator strengths (*f*) and important orbitals involved in transition for Type-III and Type-B interfaces of NH_2_DA-MOF and NH_2_F-MOF, respectively, in their stacked orientation.

Systems with C_{60}	Excited State (Ex. St.)	Excitation energies ($E_{0\text{-}n}$, eV)	Wavelength (nm)	Oscillator strengths (*f*)	Important orbitals involved
Type-III NH_2-DA Stack	1	0.62	1999.41	0.0003	H→L
	2	0.67	1849.33	0.0047	H→L+1; H→L+2
	3	0.69	1799.39	0.0054	H→L+1; H→L+2
	6	0.83	1490.67	0.0312	H-1→L; H-1→L+1; H-1→L+2
	9	1.59	781.84	0.0524	H-1→L+3; H→L+4
	10	1.62	763.43	1.0257	H-2→L+9; H-1→L+3; H→L+4
	20	1.93	642.35	0.0315	H-3→L+1; H-3→L+3; H-1→L+5; H-1→L+6
	66	2.75	451.12	0.0153	H-4→L+4
	81	2.93	423.77	0.3170	H-3→L+3; H-2→L+7; H-1→L+8

	92	2.98	416.36	0.3585	H-9→L+4; H-2→L+4; H→L+12; H→L+13
Type-B NH_2-F Stacked	1	0.51	2440.32	0.0001	H→L; H→L+1
	2	0.55	2274.70	0.0034	H→L; H→L+1; H→L+2
	3	0.59	2099.13	0.0263	H-1→L; H→L+1; H→L+2
	4	0.60	2081.01	0.0152	H-1→L; H-1→L+1; H→L+1; H→L+2
	6	0.66	1865.26	0.0288	H-1→L; H-1→L+1; H-1→L+2
	11	1.58	784.30	0.0067	H-3→L+1
	21	1.91	648.46	0.0852	H-2→L+9; H-1→L+3; H→L+4
	22	1.93	642.15	0.2893	H-1→L+3; H-1→L+6; H→L+4
	34	2.19	565.10	0.0288	H-4→L+1; H-4→L+2; H→L+9
	99	3.00	412.66	0.0108	H→L+15; H→L+16

Charge carrier and exciton migrations play a crucial role in controlling electron conduction in optoelectronic devices.[63-64] Carrier mobilities across molecular interfaces can be assessed from Marcus theory (Eq. S1 in SI) and depend on the electronic transfer integral (V) between the adjacent molecules as well as the reorganization energy (λ). Transfer integrals are extremely sensitive to the relative orientation of the associated molecules and the direction of transport. Therefore, we have considered different possible hopping pathways between adjacent molecular fragments and computed associated transfer integrals. Analyzing center-to-center distances between the nearest neighbor porphyrinic units in DA-MOF and F-MOF (and also in their analogues, but all without C_{60} incorporation), we have considered four possible pathways

namely, AB, AC, AD and AE for exciton migrations (Figure S27 in SI). Computed hole (V_h) and electron (V_e) transfer integrals are negligible in all of the pathways for both MOFs (Table S14 in SI), suggesting the electronic transport between the porphyrinic units is ineffective for conduction in the absence of a dopant of some sort.

Table3. Computed electron-transfer (V_e, cm^{-1}) and hole-transfer (V_h, cm^{-1}) integrals between porphyrin-based linkers and C_{60} along different pathways for C_{60}@DA-MOF, C_{60}@F-MOF, and their analogues.

C_{60} incorporated Systems	Interface	Pathways			
		AF V_e (V_h)	BF V_e (V_h)	CF V_e (V_h)	DF V_e (V_h)
DA-MOF	Parent	0.32 (1.05)	21.78 (82.11)	8.71 (8.79)	9.52 (24.12)
H_DA-MOF	Type-I	0.65 (11.53)	2.42 (11.13)	2.98 (1.45)	13.79 (4.60)
	Type-II	142.92 (774.29)	695.17 (306.41)	0.00 (0.00)	0.00 (0.00)
	Type-III	392.79 (687.51)	173.97 (216.40)	1.29 (0.48)	111.39 (58.39)
NH_2_DA-MOF	Type-I	0.65 (11.53)	2.42 (11.13)	2.98 (1.45)	13.79 (4.60)
	Type-II	197.44 (992.95)	669.36 (460.62)	0.00 (0.08)	0.00 (0.00)
	Type-III	207.61 (610.72)	228.66 (241.64)	0.48 (0.73)	116.55 (627.10)
F-MOF	Parent	487.32 (371.26)	534.75 (383.60)	0.08 (0.00)	0.08 (0.00)
H_F-MOF	Type-A	0.48 (109.93)	591.29	0.00 (0.00)	0.00 (0.00)

			(297.94)		
	Type-B	40.33 (72.75)	32.10 (5.40)	212.53 (129.05)	116.71 (194.06)
NH_2_F-MOF	Type-A	113.24 (100.74)	406.50 (427.55)	0.00 (0.00)	0.00 (0.00)
	Type-B	17.10 (0.32)	13.79 (31.70)	84.12 (143.89)	190.18 (410.21)

We next computed transfer integrals between donor-acceptor conjugates in the various C_{60}@MOFs considered here (Figures S28-S32 in SI) addressing four pathways, namely, AF, BF, CF and DF. Computed coupling values (V) are anisotropic in nature and highly dependent on pathway (Table 3). For C_{60}@DA-MOF, the maximum V_h and V_e values are predicted to be 82.1 and 21.8 cm^{-1}, respectively, along the BF pathway. For Type-I interfaces, where C_{60} has a similar orientation as in parent DA-MOF, we compute still lower V values, as the removal of the phenyl rings from the meso positions further decreases the π···π overlap between them (Figures S28, S29 and S31). By contrast, these values increase significantly for the Type-II interfaces of both H_DA-MOF (V_h= 774.3 cm^{-1} and V_e= 695.2 cm^{-1}) and NH_2_DA-MOF (V_h= 993.0 cm^{-1} and V_e= 669.4 cm^{-1}) due to optimal π···π stacking overlap between the porphyrin and C_{60} (Table 3). Relative to these highest values, the predicted integrals in Type-III interfaces decrease somewhat (V_h= 687.5 cm^{-1} and V_e= 392.8 cm^{-1} for H_DA-MOF and V_h= 627.1 cm^{-1} and V_e= 228.7 cm^{-1} for NH_2_DA-MOF) as might be anticipated given the the slip-stacked arrangement of C_{60} relative to the porphyrin (Figure S29 and S31). Interestingly, though, Type-III interfaces *do* provide an additional mechanism, along the DF pathway, for charge transport that is not available in the other cases.

Similarly, for C_{60}@F-MOF as well as for the Type-A polymorphs of its analogues, the largest transfer integrals are associated with ideal, eclipsed π···π stacking interaction (Table 3, Figure S28, S30 and S32). The coupling values decrease considerably for both C_{60}@H_F-MOF and C_{60}@NH_2_F-MOF Type-B polymorphs where the slip-stacked geometry is less optimal.

It is apparent, then, that computed transfer integrals increase significantly upon C_{60} incorporation in all of the MOFs considered here (cf. Table S15 in SI). Importantly, C_{60} is known to have very small reorganization energies in electron transfer reactions, which is essential for the generation of long-lived charge-separated states.[61] Taking this together with our solid-state calculations, molecular TD-DFT calculations, and computed electronic coupling values, we may posit that electrical transport will be high in C_{60} encapsulated porphyrin-based MOFs and that these will be promising materials for optoelectronics, particularly when linker modifications are chosen to enhance the likelihood of eclipsed π-π stacking interactions between the fullerene and the porphyrin.

Conclusions

The incorporation of C_{60} into the pores of porphyrin-containing DA-MOF and F-MOF analogs shows great promise for engendering massive electrical conductivity through π-mediated donor-acceptor interactions, as confirmed through calculation of electronic transfer integrals for materials with and without C_{60}. Substitution at the meso positions of the porphyrin can lead to C_{60} occupying different positions within the framework, and calculations indicate that these polymorphic heterostructures possess anisotropic structural, electronic, opto-electronic, and transport properties that depend on variable donor-acceptor interactions. TD-DFT calculations also indicate that electrons can be transferred from porphyrin to C_{60} either directly through near-infrared charge-transfer transitions or as well by photoinduced electron transfer processes upon visible light excitation. This organization could prolong the lifetime of charge separated states at interfaces and substantially improve the performance of the doped MOFs for optoelectronic applications. Our detailed insights into the structural, electronic, and photophysical properties of porphyrin-based MOFs incorporating C_{60} as guest will hopefully further stimulate the rational design of improved MOF-derived photoelectrochemical devices.

Supporting Information:

Lattice parameters, electronic structures, cluster modelling and excited states calculations results, hopping pathways and other related data, full references of Gaussian 16 and ADF.

Acknowledgment:

This research was supported by the U.S. Department of Energy, Office of Basic Energy Sciences, Division of Chemical Sciences, Geosciences and Biosciences under Award DE-FG02-17ER16362. Computer resources were provided by the Minnesota Supercomputing Institute at the University of Minnesota.

References:

1. Furukawa, H.; Cordova, K. E.; O'Keeffe, M.; Yaghi, O. M., The Chemistry and Applications of Metal-Organic Frameworks. *Science* **2013,** *341*, 1230444.
2. Corma, A.; García, H.; Llabrés i Xamena, F. X., Engineering Metal Organic Frameworks for Heterogeneous Catalysis. *Chem. Rev.* **2010,** *110*, 4606-4655.
3. Dincă, M.; Long, J. R., Hydrogen Storage in Microporous Metal–Organic Frameworks with Exposed Metal Sites. *Angew. Chem. Int. Ed.* **2008,** *47*, 6766-6779.
4. Momeni, M. R.; Cramer, C. J., Structural Characterization of Pristine and Defective $[Zr_{12}(\mu_3\text{-}O)_8(\mu_3\text{-}OH)_8(\mu_2\text{-}OH)_6]^{18+}$ Double-Node Metal–Organic Framework and Predicted Applications for Single-Site Catalytic Hydrolysis of Sarin. *Chem. Mater.* **2018,** *30*, 4432-4439.
5. Farha, O. K.; Özgür Yazaydın, A.; Eryazici, I.; Malliakas, C. D.; Hauser, B. G.; Kanatzidis, M. G.; Nguyen, S. T.; Snurr, R. Q.; Hupp, J. T., De Novo Synthesis of a Metal–Organic Framework Material Featuring Ultrahigh Surface Area and Gas Storage Capacities. *Nat. Chem.* **2010,** *2*, 944-948.
6. Zhang, T.; Lin, W., Metal–Organic Frameworks for Artificial Photosynthesis and Photocatalysis. *Chem. Soc. Rev.* **2014,** *43*, 5982-5993.
7. Zeng, L.; Guo, X.; He, C.; Duan, C., Metal–Organic Frameworks: Versatile Materials for Heterogeneous Photocatalysis. *ACS Catal.* **2016,** *6*, 7935-7947.
8. Horcajada, P.; Chalati, T.; Serre, C.; Gillet, B.; Sebrie, C.; Baati, T.; Eubank, J. F.; Heurtaux, D.; Clayette, P.; Kreuz, C.; Chang, J.-S.; Hwang, Y. K.; Marsaud, V.; Bories, P.-N.; Cynober, L.; Gil, S.; Férey, G.; Couvreur, P.; Gref, R., Porous Metal–Organic-Framework Nanoscale Carriers as a Potential Platform for Drug Delivery and Imaging. *Nat. Mater.* **2009,** *9*, 172-178.
9. Pratik, S. M.; Cramer, C. J., Predicted Efficient Visible-Light Driven Water Splitting and Carbon Dioxide Reduction Using Photoredox Active UiO-NDI Metal Organic Framework. *J. Phys. Chem. C* **2019,** *123*, 19778-19785.
10. Stavila, V.; Talin, A. A.; Allendorf, M. D., MOF-Based Electronic and Opto-Electronic Devices. *Chem. Soc. Rev.* **2014,** *43*, 5994-6010.
11. Davis, M. E., Ordered Porous Materials for Emerging Applications. *Nature* **2002,** *417*, 813-821.
12. Patwardhan, S.; Schatz, G. C., Theoretical Investigation of Charge Transfer in Metal Organic Frameworks for Electrochemical Device Applications. *J. Phys. Chem. C* **2015,** *119*, 24238-24247.
13. Choi, K. M.; Jeong, H. M.; Park, J. H.; Zhang, Y.-B.; Kang, J. K.; Yaghi, O. M., Supercapacitors of Nanocrystalline Metal–Organic Frameworks. *ACS Nano* **2014,** *8*, 7451-7457.

14. So, M. C.; Wiederrecht, G. P.; Mondloch, J. E.; Hupp, J. T.; Farha, O. K., Metal–Organic Framework Materials for Light-Harvesting and Energy Transfer. *Chem. Commun.* **2015,** *51*, 3501-3510.
15. D'Alessandro, D. M., Exploiting Redox Activity in Metal–Organic Frameworks: Concepts, Trends and Perspectives. *Chem. Commun.* **2016,** *52*, 8957-8971.
16. Dolgopolova, E. A.; Rice, A. M.; Martin, C. R.; Shustova, N. B., Photochemistry and Photophysics of MOFs: Steps towards MOF-Based Sensing Enhancements. *Chem. Soc. Rev.* **2018,** *47*, 4710-4728.
17. Hua, C.; Doheny, P. W.; Ding, B.; Chan, B.; Yu, M.; Kepert, C. J.; D'Alessandro, D. M., Through-Space Intervalence Charge Transfer as a Mechanism for Charge Delocalization in Metal–Organic Frameworks. *J. Am. Chem. Soc.* **2018,** *140*, 6622-6630.
18. Zhang, Q.; Zhang, C.; Cao, L.; Wang, Z.; An, B.; Lin, Z.; Huang, R.; Zhang, Z.; Wang, C.; Lin, W., Förster Energy Transport in Metal–Organic Frameworks Is Beyond Step-by-Step Hopping. *J. Am. Chem. Soc.* **2016,** *138*, 5308-5315.
19. Kent, C. A.; Mehl, B. P.; Ma, L.; Papanikolas, J. M.; Meyer, T. J.; Lin, W., Energy Transfer Dynamics in Metal−Organic Frameworks. *J. Am. Chem. Soc* **2010,** *132*, 12767-12769.
20. Hod, I.; Bury, W.; Gardner, D. M.; Deria, P.; Roznyatovskiy, V.; Wasielewski, M. R.; Farha, O. K.; Hupp, J. T., Bias-Switchable Permselectivity and Redox Catalytic Activity of a Ferrocene-Functionalized, Thin-Film Metal–Organic Framework Compound. *J. Phys. Chem. Lett.* **2015,** *6*, 586-591.
21. Aubrey, M. L.; Wiers, B. M.; Andrews, S. C.; Sakurai, T.; Reyes-Lillo, S. E.; Hamed, S. M.; Yu, C.-J.; Darago, L. E.; Mason, J. A.; Baeg, J.-O.; Grandjean, F.; Long, G. J.; Seki, S.; Neaton, J. B.; Yang, P.; Long, J. R., Electron Delocalization and Charge Mobility as a Function of Reduction in a Metal–Organic Framework. *Nat. Mater.* **2018,** *17*, 625-632.
22. Park, J. G.; Aubrey, M. L.; Oktawiec, J.; Chakarawet, K.; Darago, L. E.; Grandjean, F.; Long, G. J.; Long, J. R., Charge Delocalization and Bulk Electronic Conductivity in the Mixed-Valence Metal–Organic Framework Fe(1,2,3-triazolate)$_2$(BF_4)$_x$. *J. Am. Chem. Soc.* **2018,** *140*, 8526-8534.
23. Xie, L. S.; Sun, L.; Wan, R.; Park, S. S.; DeGayner, J. A.; Hendon, C. H.; Dincă, M., Tunable Mixed-Valence Doping toward Record Electrical Conductivity in a Three-Dimensional Metal–Organic Framework. *J. Am. Chem. Soc.* **2018,** *140*, 7411-7414.
24. Nie, X.; Kulkarni, A.; Sholl, D. S., Computational Prediction of Metal Organic Frameworks Suitable for Molecular Infiltration as a Route to Development of Conductive Materials. *J. Phys.Chem. Lett.* **2015,** *6*, 1586-1591.
25. Sheberla, D.; Bachman, J. C.; Elias, J. S.; Sun, C.-J.; Shao-Horn, Y.; Dincă, M., Conductive MOF Electrodes for Stable Supercapacitors with High Areal Capacitance. *Nat. Mater.* **2016,** *16*, 220-224.
26. Sheberla, D.; Sun, L.; Blood-Forsythe, M. A.; Er, S.; Wade, C. R.; Brozek, C. K.; Aspuru-Guzik, A.; Dincă, M., High Electrical Conductivity in Ni_3(2,3,6,7,10,11-hexaiminotriphenylene)$_2$, a Semiconducting Metal–Organic Graphene Analogue. *J. Am. Chem. Soc.* **2014,** *136*, 8859-8862.
27. Shiozawa, H.; Bayer, B. C.; Peterlik, H.; Meyer, J. C.; Lang, W.; Pichler, T., Doping of Metal–Organic Frameworks towards Resistive Sensing. *Sci. Rep.* **2017,** *7*, 2439.
28. Allendorf, M. D.; Foster, M. E.; Léonard, F.; Stavila, V.; Feng, P. L.; Doty, F. P.; Leong, K.; Ma, E. Y.; Johnston, S. R.; Talin, A. A., Guest-Induced Emergent Properties in Metal–Organic Frameworks. *J. Phys. Chem. Lett.* **2015,** *6*, 1182-1195.

29. Leong, C. F.; Chan, B.; Faust, T. B.; D'Alessandro, D. M., Controlling Charge Separation in a Novel Donor–Acceptor Metal–Organic Framework Via Redox Modulation. *Chem. Sci.* **2014,** *5*, 4724-4728.
30. Talin, A. A.; Centrone, A.; Ford, A. C.; Foster, M. E.; Stavila, V.; Haney, P.; Kinney, R. A.; Szalai, V.; El Gabaly, F.; Yoon, H. P.; Léonard, F.; Allendorf, M. D., Tunable Electrical Conductivity in Metal-Organic Framework Thin-Film Devices. *Science* **2014,** *343*, 66-69.
31. Kung, C.-W.; Otake, K.; Buru, C. T.; Goswami, S.; Cui, Y.; Hupp, J. T.; Spokoyny, A. M.; Farha, O. K., Increased Electrical Conductivity in a Mesoporous Metal–Organic Framework Featuring Metallacarboranes Guests. *J. Am. Chem. Soc.* **2018,** *140*, 3871-3875.
32. Goswami, S.; Ray, D.; Otake, K.-i.; Kung, C.-W.; Garibay, S. J.; Islamoglu, T.; Atilgan, A.; Cui, Y.; Cramer, C. J.; Farha, O. K.; Hupp, J. T., A Porous, Electrically Conductive Hexa-Zirconium(Iv) Metal–Organic Framework. *Chem. Sci.* **2018,** *9*, 4477-4482.
33. Williams, D. E.; Dolgopolova, E. A.; Godfrey, D. C.; Ermolaeva, E. D.; Pellechia, P. J.; Greytak, A. B.; Smith, M. D.; Avdoshenko, S. M.; Popov, A. A.; Shustova, N. B., Fulleretic Well-Defined Scaffolds: Donor–Fullerene Alignment Through Metal Coordination and Its Effect on Photophysics. *Angew. Chem. Int. Ed.* **2016,** *55*, 9070-9074.
34. Chen, L.; Furukawa, K.; Gao, J.; Nagai, A.; Nakamura, T.; Dong, Y.; Jiang, D., Photoelectric Covalent Organic Frameworks: Converting Open Lattices into Ordered Donor–Acceptor Heterojunctions. *J. Am. Chem. Soc.* **2014,** *136*, 9806-9809.
35. Liu, X.; Kozlowska, M.; Okkali, T.; Wagner, D.; Higashino, T.; Brenner-Weiß, G.; Marschner, S. M.; Fu, Z.; Zhang, Q.; Imahori, H.; Bräse, S.; Wenzel, W.; Wöll, C.; Heinke, L., Photoconductivity in Metal–Organic Framework (MOF) Thin Films. *Angew. Chem. Int. Ed.* **2019,** *58*, 9590-9595.
36. Manuel, S.; Joaquín, C.; Samuel, M.-V.; Aron, W.; Guillermo, M. E., Investigation of Charge-Transfer Interactions Induced by Encapsulating Fullerene in a Mesoporous Tetrathiafulvalene-Based Metal-Organic Framework. **2019**, DOI: 10.26434/chemrxiv.8427047.v1.
37. Walter, M. G.; Rudine, A. B.; Wamser, C. C., Porphyrins and Phthalocyanines in Solar Photovoltaic Cells. *J. Porphyrins Phthalocyanines* **2010,** *14*, 759-792.
38. Li, L.-L.; Diau, E. W.-G., Porphyrin-Sensitized Solar Cells. *Chem. Soc. Rev.* **2013,** *42*, 291-304.
39. Pratik, S. M.; Datta, A., Computational design of concomitant type-I and type-II porphyrin sensitized solar cells. *Phys. Chem. Chem. Phys.* **2013,** *15*, 18471-18481.
40. So, M. C.; Jin, S.; Son, H.-J.; Wiederrecht, G. P.; Farha, O. K.; Hupp, J. T., Layer-by-Layer Fabrication of Oriented Porous Thin Films Based on Porphyrin-Containing Metal–Organic Frameworks. *J. Am. Chem. Soc.* **2013,** *135*, 15698-15701.
41. Hod, I.; Sampson, M. D.; Deria, P.; Kubiak, C. P.; Farha, O. K.; Hupp, J. T., Fe-Porphyrin-Based Metal–Organic Framework Films as High-Surface Concentration, Heterogeneous Catalysts for Electrochemical Reduction of CO_2. *ACS Catal.* **2015,** *5*, 6302-6309.
42. He, T.; Chen, S.; Ni, B.; Gong, Y.; Wu, Z.; Song, L.; Gu, L.; Hu, W.; Wang, X., Zirconium–Porphyrin-Based Metal–Organic Framework Hollow Nanotubes for Immobilization of Noble-Metal Single Atoms. *Angew. Chem. Int. Ed.* **2018,** *57*, 3493-3498.
43. Liu, J.; Zhou, W.; Liu, J.; Howard, I.; Kilibarda, G.; Schlabach, S.; Coupry, D.; Addicoat, M.; Yoneda, S.; Tsutsui, Y.; Sakurai, T.; Seki, S.; Wang, Z.; Lindemann, P.; Redel, E.; Heine, T.; Wöll, C., Photoinduced Charge-Carrier Generation in Epitaxial MOF Thin Films: High

Efficiency as a Result of an Indirect Electronic Band Gap? *Angew. Chem.Int. Ed.* **2015,** *54*, 7441-7445.
44. Hamad, S.; Hernandez, N. C.; Aziz, A.; Ruiz-Salvador, A. R.; Calero, S.; Grau-Crespo, R., Electronic Structure of Porphyrin-Based Metal–Organic Frameworks and Their Suitability for Solar Fuel Production Photocatalysis. *J. Mater. Chem. A* **2015,** *3*, 23458-23465.
45. Fateeva, A.; Chater, P. A.; Ireland, C. P.; Tahir, A. A.; Khimyak, Y. Z.; Wiper, P. V.; Darwent, J. R.; Rosseinsky, M. J., A Water-Stable Porphyrin-Based Metal–Organic Framework Active for Visible-Light Photocatalysis. *Angew. Chem. Int. Ed.* **2012,** *51*, 7440-7444.
46. Son, H.-J.; Jin, S.; Patwardhan, S.; Wezenberg, S. J.; Jeong, N. C.; So, M.; Wilmer, C. E.; Sarjeant, A. A.; Schatz, G. C.; Snurr, R. Q.; Farha, O. K.; Wiederrecht, G. P.; Hupp, J. T., Light-Harvesting and Ultrafast Energy Migration in Porphyrin-Based Metal–Organic Frameworks. *J. Am. Chem. Soc.* **2013,** *135*, 862-869.
47. Jin, S.; Son, H.-J.; Farha, O. K.; Wiederrecht, G. P.; Hupp, J. T., Energy Transfer from Quantum Dots to Metal–Organic Frameworks for Enhanced Light Harvesting. *J. Am. Chem. Soc.* **2013,** *135*, 955-958.
48. Kresse, G.; Hafner, J., Ab Initio Molecular-Dynamics Simulation of the Liquid-Metal-Amorphous-Semiconductor Transition in Germanium. *Phys. Rev. B* **1994,** *49*, 14251-14269.
49. Perdew, J. P.; Ruzsinszky, A.; Csonka, G. I.; Vydrov, O. A.; Scuseria, G. E.; Constantin, L. A.; Zhou, X.; Burke, K., Restoring the Density-Gradient Expansion for Exchange in Solids and Surfaces. *Phys. Rev. Lett.* **2008,** *100*, 136406.
50. Krukau, A. V.; Vydrov, O. A.; Izmaylov, A. F.; Scuseria, G. E., Influence of the Exchange Screening Parameter on the Performance of Screened Hybrid Functionals. *J. Chem. Phys.* **2006,** *125*, 224106.
51. Grimme, S.; Antony, J.; Ehrlich, S.; Krieg, H., A Consistent and Accurate Ab Initio Parametrization of Density Functional Dispersion Correction (DFT-D) for the 94 Elements H-Pu. *J. Chem. Phys.* **2010,** *132*, 154104.
52. Hehre, W. J.; Ditchfield, R.; Pople, J. A., Self—Consistent Molecular Orbital Methods. XII. Further Extensions of Gaussian—Type Basis Sets for Use in Molecular Orbital Studies of Organic Molecules. *J. Chem. Phys.* **1972,** *56*, 2257-2261.
53. Dolg, M.; Stoll, H.; Preuss, H., Energy-Adjusted Ab Initio Pseudopotentials for the Rare Earth Elements. *J. Chem. Phys.* **1989,** *90*, 1730-1734.
54. Frisch, M. J. *Gaussian 16 Rev. B.01*, Wallingford, CT, 2016.
55. te Velde, G.; Bickelhaupt, F. M.; Baerends, E. J.; Fonseca Guerra, C.; van Gisbergen, S. J. A.; Snijders, J. G.; Ziegler, T., Chemistry with ADF. *J. Comput. Chem.* **2001,** *22*, 931-967.
56. Senthilkumar, K.; Grozema, F. C.; Bickelhaupt, F. M.; Siebbeles, L. D. A., Charge Transport in Columnar Stacked Triphenylenes: Effects of Conformational Fluctuations on Charge Transfer Integrals and Site Energies. *J. Chem. Phys.s* **2003,** *119*, 9809-9817.
57. Zhao, Y.; Truhlar, D. G., The M06 Suite of Density Functionals for Main Group Thermochemistry, Thermochemical Kinetics, Noncovalent Interactions, Excited States, and Transition Elements: Two New Functionals and Systematic Testing of Four M06-Class Functionals and 12 Other Functionals. *Theor. Chem. Acc.* **2008,** *120*, 215-241.
58. Camacho Gonzalez, J.; Mondal, S.; Ocayo, F.; Guajardo-Maturana, R.; Muñoz-Castro, A., Nature of C_{60} and C_{70} Fullerene Encapsulation in a Porphyrin- and Metalloporphyrin-Based Cage: Insights from Dispersion-Corrected Density Functional Theory Calculations. *Int. J. Quantum Chem.* **2020,** *120*, e26080.

59. Urbani, M.; Grätzel, M.; Nazeeruddin, M. K.; Torres, T., Meso-Substituted Porphyrins for Dye-Sensitized Solar Cells. *Chem. Rev.* **2014,** *114*, 12330-12396.
60. Sukegawa, J.; Schubert, C.; Zhu, X.; Tsuji, H.; Guldi, D. M.; Nakamura, E., Electron Transfer Through Rigid Organic Molecular Wires Enhanced by Electronic and Electron–Vibration Coupling. *Nat. Chem.* **2014,** *6*, 899-905.
61. D'Souza, F.; Ito, O., Photoinduced Electron Transfer in Supramolecular Systems of Fullerenes Functionalized with Ligands Capable of Binding to Zinc Porphyrins and Zinc Phthalocyanines. *Coord. Chem. Rev.* **2005,** *249*, 1410-1422.
62. Guldi, D. M.; Hirsch, A.; Scheloske, M.; Dietel, E.; Troisi, A.; Zerbetto, F.; Prato, M., Modulating Charge-Transfer Interactions in Topologically Different Porphyrin–C_{60} Dyads. *Chem. Eur. J.* **2003,** *9*, 4968-4979.
63. Brédas, J.-L.; Beljonne, D.; Coropceanu, V.; Cornil, J., Charge-Transfer and Energy-Transfer Processes in π-Conjugated Oligomers and Polymers: A Molecular Picture. *Chem. Rev.* **2004,** *104*, 4971-5004.
64. Wen, S.-H.; Li, A.; Song, J.; Deng, W.-Q.; Han, K.-L.; Goddard, W. A., First-Principles Investigation of Anistropic Hole Mobilities in Organic Semiconductors. *J. Phys. Chem. B* **2009,** *113*, 8813-8819.

TOC Graphic: